Exp Fluids (2014) 55:1670
DOI 10.1007/s00348-014-1670-3

RESEARCH ARTICLE

Digital in-line holography to quantify secondary droplets from the impact of a single drop on a thin film

Daniel R. Guildenbecher · Luke Engvall · Jian Gao · Thomas W. Grasser · Phillip L. Reu · Jun Chen

Received: 2 August 2013 / Revised: 18 October 2013 / Accepted: 14 January 2014 / Published online: 15 March 2014

Abstract Digital in-line holography (DIH) is an optical technique which measures particle sizes and their three-dimensional (3D) positions and velocities. Here DIH and a recently proposed hybrid method of particle detection are applied to quantify the secondary droplets generated by the impact of a single drop on a thin film. By leveraging the expected symmetry between in-plane and out-of-plane velocities, experimental depth uncertainty is measured to be approximately 0.7 of the mean droplet diameter. Furthermore, comparison with previous measurements using alternative techniques shows good agreement with the measured temporal evolution of drop number, size, and velocity components. Finally, the power of DIH to extract the complex 3D morphology of the protruding jets is demonstrated.

1 Introduction

Digital in-line holography (DIH) is an optical technique in which a collimated laser illuminates an object field. The resulting diffraction pattern is digitally recorded, and numerical reconstruction of the volumetric field is performed via solution of the diffraction integral equations (Schnars and Jueptner 2005; Katz and Sheng 2010). DIH has a number of advantages for quantification of multi-phase, particle flows including: (1) individual particles can be located in three-dimensional (3D) space; (2) the size and shape of each particle can be measured at their in-focus location; (3) 3D particle velocities can be determined from two or more holograms recorded with short interframe time intervals; (4) non-spherical particles can be quantified; and (5) knowledge of the index of refraction is not necessarily required. Due to these advantages, DIH has been explored for applications to flows of gaseous particulates (Tian et al. 2010; Lebrun et al. 2011), liquid particulates (Gire et al. 2008; Gopalan and Katz 2010; Yang et al. 2012), and solid particulates (Khanam et al. 2011; Spuler and Fugal 2011; Wu et al. 2011), among many others.

Specific challenges in DIH include the following: (1) a large depth of focus caused by the limited angular aperture, (2) noise caused by an out-of-focus twin image, and (3) difficulty separating particles which overlap in the field of view. In attempting to overcome these challenges, a number of methods have been proposed to reconstruct the light field and extract the in-focus particle locations and shapes (Gire et al. 2008; Tian et al. 2010; Yang et al. 2012). Recently, we have proposed a new technique, which combines some of these previous methods (Guildenbecher et al. 2012, 2013a; Gao et al. 2013a). Our new hybrid method reduces the reliance on tunable, user-defined parameters and has been specifically designed for automatic detection of non-spherical particles. Accuracy has been verified through simulations and experiments with stationary particle fields illuminated by continuous lasers (Guildenbecher et al. 2013a; Gao et al. 2013a). Furthermore, when pulsed lasers are used to freeze motion, experiments have been performed which confirm no significant loss in accuracy (Guildenbecher et al. 2013b). Finally, the method has been applied to quantify the breakup of a drop in an aerodynamic flow where it was used to successfully extract the 3D volume of the highly

D. R. Guildenbecher (✉) · L. Engvall · T. W. Grasser · P. L. Reu
Sandia National Laboratories, Albuquerque, NM, USA
e-mail: drguild@sandia.gov

J. Gao · J. Chen
Purdue University School of Mechanical Engineering, West Lafayette, IN, USA

non-spherical, ring-shaped ligament which develops during the breakup process (Gao et al. 2013b).

In this work, DIH and the hybrid method are applied to quantify the spatial and temporal properties of secondary drops produced from the impact of a single drop on a thin film. This process has been widely studied for applications to fuel sprays in combustion engines with reviews provided by Yarin (2006) and Moreira et al. (2010); however, only limited experimental investigations of secondary droplet sizes and velocities are available. This lack of data can be at least partially attributed to difficulties obtaining spatially and temporally converged statistics using point-wise phase Doppler anemometer (PDA) (Samenfink et al. 1999) or shadowgraphy focused on a two-dimensional (2D) plane (Cossali et al. 2004; Okawa et al. 2006; Richter et al. 2005). Unlike these techniques, DIH provides 3D quantification of the secondary droplet plume from a single hologram; therefore, converged statistics can be obtained from reduced experimental repetition.

When a spherical drop impacts on a thin film, the mean properties of the secondary droplet field are expected to be rotationally symmetric assuming sufficient data are obtained for converged statistics. Consequently, the 3D field of view provided by DIH is not entirely necessary to resolve the mean properties of the secondary droplets. However, as is shown in subsequent sections, this symmetry also presents opportunities to compare the detected 3D velocity components and quantify experimental depth uncertainty. Consequently, the drop impact process is a good initial configuration to quantify the experimental accuracy of DIH and the hybrid method before application to more complex, 3D processes which cannot be easily quantified by other means.

This work begins with an overview of DIH and the hybrid method. This is followed by the experimental configuration for quantification of drop impact on a thin film using DIH. Next, secondary drop sizes and velocities are measured from the experimental holograms, and process symmetry is used to estimate out-of-plane uncertainties. Finally, comparison of experimental results with published values verifies the accuracy of the DIH measurements.

2 Digital in-line holography and the hybrid method

In-depth reviews of DIH methodology (Schnars and Jueptner 2005; Katz and Sheng 2010) and detailed discussion on the hybrid processing method (Guildenbecher et al. 2012, 2013a, b; Gao et al. 2013a) can be found elsewhere. Here, some specifics of the techniques are presented for the purposes of introduction and to aid the reader during the discussion of the experimental results to follow.

An in-line hologram records the interference between a reference beam and a portion of the beam scattered by droplets in its path. After an experiment, multiplication of the digitally recorded hologram, H, with the conjugate reference wave, E_r^*, yields an estimate of the conjugate object wave. This in turn can be numerically propagated to a specified depth, z, through solution of the diffraction equation.

$$E(x,y;z) = \left[H(x,y)E_r^*(x,y)\right] \otimes g(x,y;z). \quad (1)$$

Here, E is the reconstructed complex amplitude; x, y are the spatial coordinates in the hologram plane; $\otimes$ represents the convolution operation; and g is the diffraction kernel (Schnars and Jueptner 2005; Katz and Sheng 2010). Equation (1) is numerically evaluated using the convolution theorem and the fast Fourier transform to find $E(x,y;z)$ at any z. The reconstructed light field is visualized using its amplitude, $A = |E|$, or intensity, $I = |E|^2$. In this work, the reference wave is assumed to be a uniform, planar beam such that $E_r^* = 1$.

While most applications of DIH utilize Eq. (1) (or some close equivalent) to numerically refocus the recorded hologram, significant differences exist in the software algorithms used to locate the z-location of in-focus droplets and extract droplet morphology. In the hybrid method, in-focus droplets are assumed to be defined by regions which display a minimum in intensity and a maximum in edge sharpness with respect to z. Here, edge sharpness is defined by the Tenengrad operator,

$$T(x,y;z) = \left[A(x,y;z) \otimes S_x\right]^2 + \left[A(x,y;z) \otimes S_y\right]^2 \quad (2)$$

where S_x and S_y are the horizontal and vertical Sobel kernels, respectively.

To begin, the hologram is numerically refocused to 1,001 different z-positions over a range which encompasses the expected droplet locations. From this, a minimum intensity image, $I_{\min}$, maximum Tenengrad image, $T_{\max}$, and z-location of maximum Tenengrad, z_{Tmax}, are calculated as,

$$I_{\min}(x,y) = \min_z I(x,y;z), \quad (3)$$

$$T_{\max}(x,y) = \max_z T(x,y;z), \quad (4)$$

$$z_{Tmax}(x,y) = \arg\max_z T(x,y;z). \quad (5)$$

A family of possible droplet shapes is found by thresholding $I_{\min}$ at 100 different values such that connected regions below the threshold define the possible droplet shapes. For each possible droplet shape, the average value of $T_{\max}$ along the exterior edge pixels is calculated and the in-focus droplet shape is taken from the threshold where this value maximizes. Finally, the z-location of the droplet is found from the average value of z_{Tmax} along the exterior

edge pixels of the in-focus shape. To further increase the accuracy of the detected droplet morphologies and z-positions, the process is repeated a second time using the local intensity, I, reconstructed at the initial estimate of the droplet z-position in place of $I_{\min}$.

These equations are implemented in a custom MATLAB script. Processing of a single hologram (4,872 × 3,248 pixels) requires approximately 30 min on a PC with dual Intel Xenon E5-2665 processors and roughly 8 gigabytes of available memory. Code optimization has not been the focus of work to-date, and reduction in processing time and memory requirements is likely possible. For these purposes, graphical processing units (GPU) are particularly promising but have not yet been fully explored.

3 Experimental configuration

The experimental configuration for investigation of drop impact on a thin film is illustrated in Fig. 1. Similar to Cossali et al. (2004), liquid drops are produced from deionized water using a droplet generator consisting of a syringe pump and syringe tip. Individual drops leave the syringe tip with approximately zero velocity and are accelerated due to gravity before impacting the center of a thin film also made of deionized water. The film is held inside a rubber o-ring with square cross-section affixed to a smooth acrylic surface. Visual observations indicate that the thickness of the film, h, is equal to that of the o-ring ($h = 2.35$ mm), and the extent of the film (50.8 mm diameter) is sufficiently large to prevent interaction of its edges with the breakup process. Finally, the drop production rate is sufficiently slow (on the order of 1 Hz) such that the conditions considered here can be assumed equivalent to the impact of an individual drop on an infinite, initially quiescent thin film.

A double-pulsed Continuum MiniLite PIV laser (frequency-doubled Nd:YAG, 532-nm center wavelength, 5-ns pulse duration, 15 Hz maximum rep-rate) provides the reference beam for the DIH system. As shown in Fig. 1, the beam first passes through a variable attenuator consisting of a half wave plate (hwp) and plate polarizer (pp). In an experiment, the output pulse energies are on the order of a few millijoules. Next, the beam is spatially filtered and further expanded in a Galilean beam expander to a final diameter of 50.8 mm. Among the various beam forming options considered, this configuration is found to be relatively compact while avoiding air-breakdown which occurs when expansion through the spatial filter is more rapid. The collimated beam passes through the secondary droplet field created by impact of the drop on the film. Finally, the scattered object waves and remaining collimated light propagate an additional 300 mm before the resulting interference pattern is recorded by a lensless CCD (Redlake EC16000 MegaPlus II monochrome camera, 4,872 × 3,248 pixels, 7.4 μm pixel pitch). Timing is achieved with a helium–neon (HeNe) laser and a photodiode placed immediately below the syringe tip. Falling drops block the HeNe beam, triggering acquisition of the holograms after an adjustable delay.

In addition to DIH, the impact process is also recorded by high-speed shadowgraphy (Phantom v7.3, 6600 frames per second, 2-μs exposure time, not shown in Fig. 1). Once again, the HeNe beam block is used to initialize recording. The field of view, as measured with a calibration grid, is 49 × 37 mm.

4 Experimental results and discussion

4.1 Initial conditions

In an experiment, the fall height (distance between the syringe tip and film) is adjusted to alter the initial impact velocity. At a given fall height, ten high-speed videos of the impact process are recorded. From these videos, the initial drop diameter, d_0, impact time since trigger, t_0, and impact velocity, v_0, are measured. These quantities are used

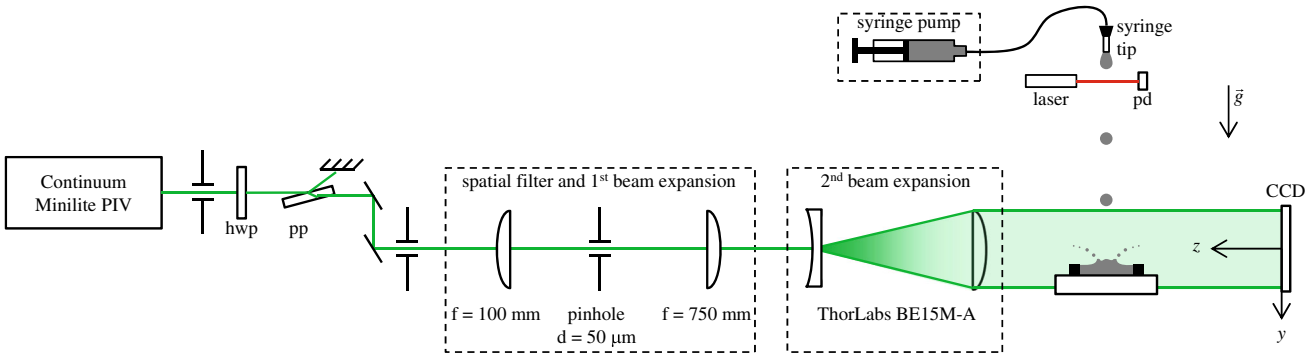

Fig. 1 Experimental configuration for DIH of drop impact on a thin film, *hwp* half wave plate, *pp* polarizing plate, *pd* photodiode

Table 1 Experimental conditions measured from backlit shadowgraphy, given as mean ± standard deviation

Approximate fall height (mm)	Initial diameter, d_0 (mm)	Impact time, t_0 (ms)	Impact velocity, v_0 (m/s)	Dimensionless film thickness, δ	Impact Weber number, *We*
530	3.21 ± 0.06	299.7 ± 0.4	3.10 ± 0.08	0.732 ± 0.007	428 ± 4
905	3.18 ± 0.02	401.0 ± 0.4	4.05 ± 0.09	0.739 ± 0.005	722 ± 5

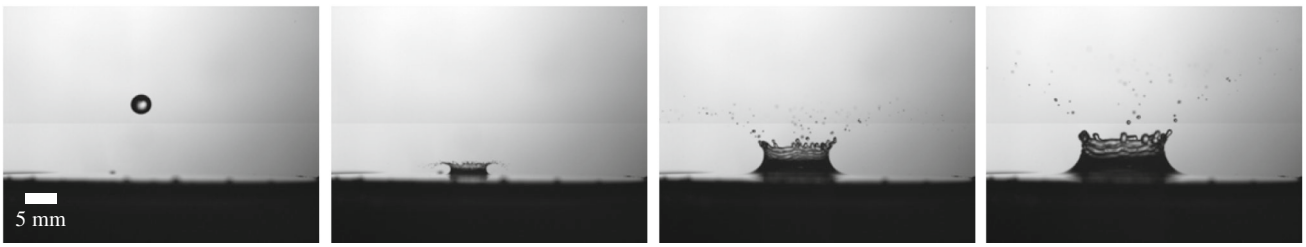

(a) τ = -2.1 **(b)** τ = 1.7 **(c)** τ = 5.5 **(d)** τ = 9.3

Fig. 2 Selected images from high-speed shadowgraphy recorded at *We* = 722

to determine the non-dimensional film height, $\delta = h/d_0$, and the impact Weber number, $We = \rho v_0^2 d_0/\sigma$, where ρ and σ are the drop density and surface tension, respectively. Here, ρ and σ are assumed equal to 1,000 kg/m^3 and 0.072 N/m, respectively.

Two different fall heights are considered, and the measured initial impact conditions are summarized in Table 1, where values are given as the mean ± standard deviation from the ten videos. In addition, Fig. 2 shows selected images from a typical high-speed video at *We* = 722. Non-dimensional time, τ, is defined as $\tau = (t-t_0)v_0/d_0$. These videos clearly show the evolution and breakup of the crown into multiple fine drops. However, due to the small depth of focus, many of the secondary drops appear out of focus. Consequently, attempts to measure secondary drop properties from these images are subject to uncertainties, which are difficult to quantify. DIH, on the other hand, records information on both the amplitude and phase of the scattered object waves. This allows for numerical refocusing and a much greater depth of field.

4.2 Holography reconstruction

In an experiment, a pair of holograms is captured with an interframe time, Δt, determined by an adjustable delay between the two laser pulses. For all conditions considered here, $\Delta t = 33$ μs. Furthermore, to capture the temporal breakup process, multiple pairs of holograms are recorded with various delay times after triggering of the HeNe beam block. For each condition defined in Table 1, seven different delay times are considered. Finally, to quantify variability and achieve converged statistics, twenty hologram pairs are recorded for each delay time.

Figure 3a shows a typical hologram recorded at *We* = 722, τ = 1.7. Diffraction patterns created from interaction of the collimated laser beam with the film, crown, and secondary droplets are recognized. Using the known properties of the laser and CCD, the hologram can be numerically refocused to a *z*-depth by solving Eq. (1). For example, Fig. 3b shows a two-dimensional (2D) visualization of the crown, cropped from the reconstruction at $z = 320$ mm.

Each hologram is processed using the hybrid method as described in Sect. 2. The method automatically extracts the *x*, *y*, *z* location of each secondary droplet, along with their 2D morphology in the *x*–*y* plane. The equivalent droplet diameter, *d*, is defined from the circle with same area as the detected 2D morphology. To minimize detection of false particles due to noise, no region is accepted with $d \leq 10$ μm. Furthermore, to determine the individual droplet velocities, matching is performed between the reconstructed droplet fields, such that 3D droplet velocity vectors are given by $\boldsymbol{v} = \Delta\boldsymbol{x}/\Delta t$ where $\Delta\boldsymbol{x}$ is the change in detected position. Here, matching is performed using a Hungarian routine from Tinevez (2012). No match is accepted where $|\Delta\boldsymbol{x}| > 0.7$ mm or the change in *d* is greater than 20 %.

Figure 3c shows a 3D representation of the measured secondary droplets. To illustrate the potential to measure complex, 3D morphology, this figure also shows features of the protruding jets, which have been extracted from the hologram. The 3D morphology of each jet is determined by the method described in Gao et al. (2013b). Briefly, the jet

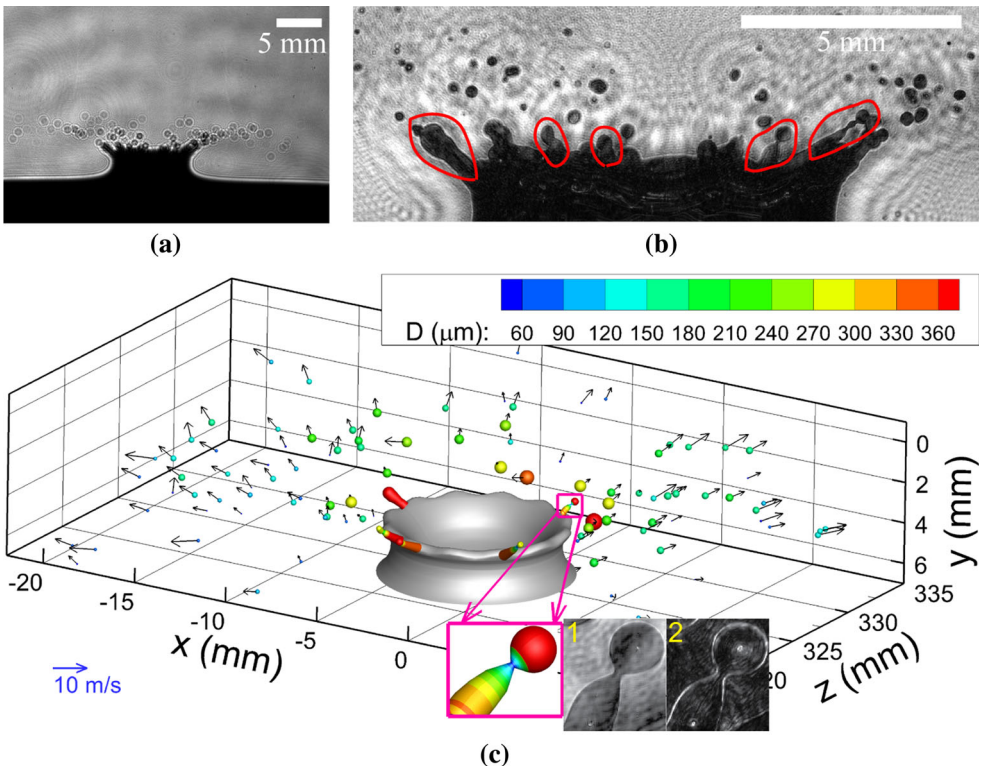

Fig. 3 **a** Typical hologram of drop impact at $We = 722$, $\tau = 1.7$, **b** reconstructed image of the crown at $z = 320$ mm, and **c** 3D representation of the measured morphology of the jets and secondary drop sizes and velocities. *Circled* in **b** are the jets whose morphologies are extracted in (**c**). *Insert 1* reconstructed image of the jet. *Insert 2* maximum sharpness image of the jet, T_{max}

is assumed to consist of differential tube segments with circular cross-section. The edge pixels of each segment are manually extracted from T_{max} as shown in the insert. The depth map, z_{Tmax}, gives the 3D coordinate of each edge pixel, from which the diameter, center location, and orientation of each segment are measured. Assuming rotational symmetry and some necessary data smoothing, individual segments are connected together to produce the measured jet. The five jets circled in Fig. 3b are extracted using this method. These are chosen because they are well distinguished from neighboring jets and other droplets. Finally, to orientate the flow, an estimated shape of the basal crown is shown in gray. This has been estimated from the 2D crown profile observed in reconstructed images, such as Fig. 3b, combined with assumed rotational symmetry. Note, the crown thickness, rim shape, and internal geometry have not been measured and estimated geometries are shown. In general, DIH is currently not capable of measuring internal features of this nature.

Figure 4 shows the 3D plot of the impact viewed from the z- and y-directions. The x–y velocities of the droplets coincide qualitatively with the observations from the high-speed video, indicating a relatively small uncertainty in the measurement of x–y velocities. Due to the large depth of focus of individual particles in DIH (Katz and Sheng 2010; Meng et al. 2004), the uncertainty of the reconstructed z-position and velocity is expected to be significantly greater than the x–y velocities, and several erroneous z-velocities

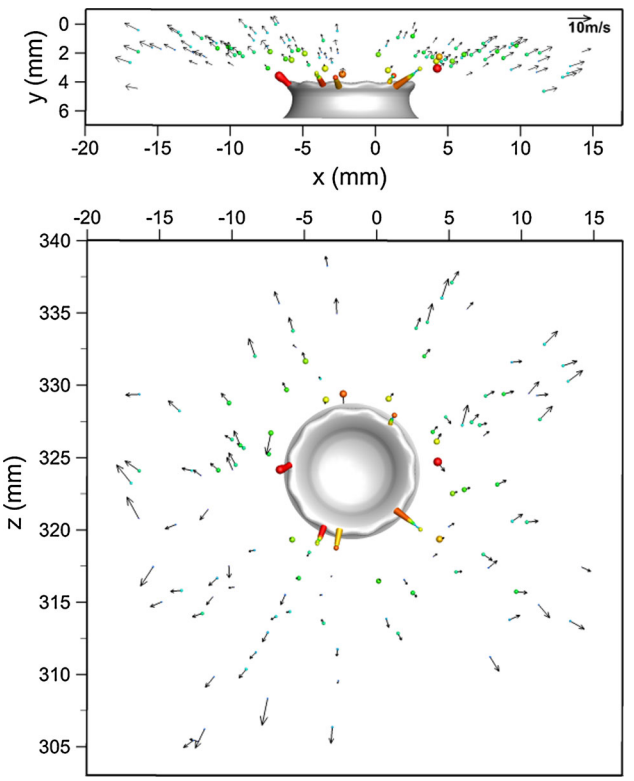

Fig. 4 3D representation of the results shown in Fig. 3c plotted in the x–y and x–z planes. Note the observed symmetry with higher uncertainty in the z-direction

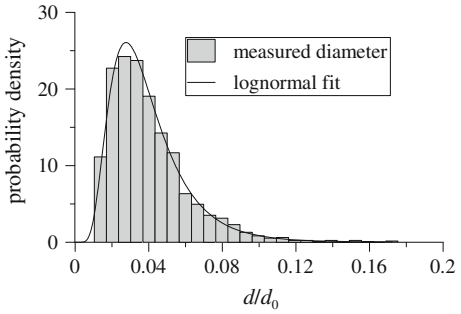

Fig. 5 Measured drop size probability density function for $We = 722$, $\tau = 1.7$

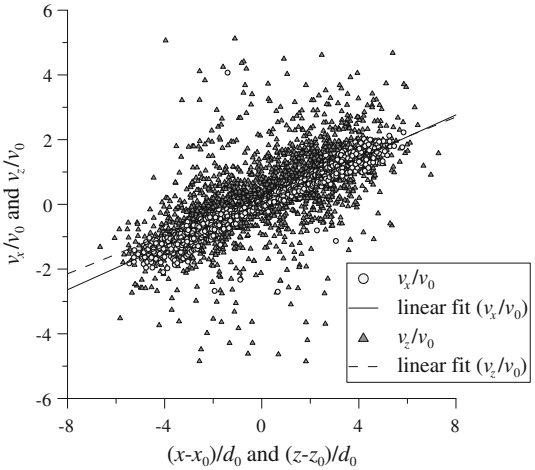

Fig. 6 Measured non-dimensional particle velocities in the x-direction, v_x/v_0, plotted as a function of x-distance from the mean, $(x–x_0)/d_0$, and in the z-direction, v_z/v_0, plotted as a function of z-distance from the mean, $(z–z_0)/d_0$, for $We = 722$, $\tau = 1.7$; note, increased scatter in the z-direction is indicative of higher measurement uncertainty in this direction

can be found by visual inspection. Nevertheless, on average symmetry of z-velocity appears qualitatively correct. Finally, the droplets are distributed radially with respect to the center of the crown, and a correlation between the magnitude of the velocity and the distance to the center of the crown is apparent.

From the single realization shown in Figs. 3 and 4, 138 droplets are detected from the first frame and 136 droplets from the second frame. To improve convergence of drop size and velocity statistics, twenty double frame realizations are recorded and reconstructed at this condition. In total 7,830 droplets are detected. From this, Fig. 5 shows the measured drop size probability density and the best-fit log-normal distribution. Importantly, the measured probability density tends toward zero at the limit of large and small diameters. This observation indicates that DIH has captured all of the relevant drop sizes and provides confidence in the mean drop sizes reported in the next subsection. Note, in some previous applications of DIH to multiphase flow, measured distributions did not capture the tail-off at small diameters (Tian et al. 2010) indicating that the optical setup or reconstruction routines were unable to capture the smallest particles within the flow. To improve the lower limit of detectible drop sizes, magnifying lenses can be used (Gao et al. 2013b), although no magnification is required here.

Figure 6 shows the x- and z-velocity components from all measured secondary droplets at $We = 722$, $\tau = 1.7$. In this figure, the non-dimensional x-velocity, v_x/v_0, is plotted as a function of non-dimensional x-distance from the mean, $(x–x_0)/d_0$, where x_0 is the mean x-position of all droplets detected at this condition. Likewise, the non-dimensional z-velocity, v_z/v_0, is plotted as a function of non-dimensional z-distance from the mean, $(z–z_0)/d_0$, where z_0 is the mean z-position of all droplets detected at this condition. Assuming, x_0, z_0 is a good estimate of the mean impact location, process symmetry dictates that, on average, the x- and z-velocity components in Fig. 6 should overlay one another, and linear fits to v_x/v_0 and v_z/v_0, also shown in Fig. 6, indicate that this is indeed true. This observation increases confidence in the mean velocities reported in the next subsection.

Because absolute droplet x, y, z positions cannot be independently measured, it is difficult to quantify depth uncertainty from the absolute measured positions. Due to this challenge, DIH depth uncertainty is often quantified using simulated holograms with known particle positions. However, simulations are unlikely to capture all relevant sources of experimental uncertainty. Alternatively, when symmetry is expected, the change in measured position between two holograms recorded with a short Δt can be used to quantify the experimental depth uncertainty. For the results in Fig. 6, model error is defined as the difference between the measured velocity component and the velocity predicted by the linear fit at the measured position. With this, the standard deviation of model errors are found to be 0.224 and 1.036 for v_x/v_0 and v_z/v_0, respectively. Assuming negligible x-positional uncertainty, the difference in standard deviation can be assumed to give DIH depth uncertainty. Velocity uncertainty is converted to positional uncertainty by multiplying by $v_0 \cdot \Delta t$. For comparison with other results in the literature, the uncertainty is re-normalized by the mean measured diameter at this condition ($\bar{d} = 0.151$ mm), resulting in an estimated standard deviation of z-positional uncertainty of $0.72 \cdot \bar{d}$.

In Guildenbecher et al. (2013a), the experimental depth uncertainty of DIH and the hybrid reconstruction method is quantified from holograms of stationary particle fields recorded with known displacements. There, an uncertainty of $1.74 \cdot \bar{d}$ is reported. Given the differences in the

experimental configuration and the methods used to quantify uncertainty, the agreement between Guildenbecher et al. (2013a) and the current work is quite reasonable. Combined, these results indicate that the depth uncertainty can be expected to be on the order of one to two particle diameters.

4.3 Comparison with previous results

The results discussed in the previous subsection are for $We = 722$, $\tau = 1.7$. Results obtained at all other time points and conditions defined in Table 1 show similar trends. To further validate these results and draw new insights into the drop breakup process, this subsection compares the experimental DIH results with previous experiments and theories.

Cossali et al. (2004) report an experimental investigation of the impact of a drop on a thin film using a configuration similar to that shown on Fig. 1. In Cossali et al. (2004), shadowgrams of the process are recorded—similar to Fig. 2—from which the number and size of secondary drops are measured using commercial software. To ease comparison, the conditions investigated here (Table 1) are made to match the conditions of Cossali et al. (2004) as closely as possible. Both investigations utilize water for the drop and the film. In Cossali et al. (2004), the initial drop diameter is approximately 3.8 mm and the film thickness ranges between 1.1 to 4.3 mm, which is similar to conditions considered here ($d_0 = 3.2$ mm, $h = 2.4$ mm). Finally, in Cossali et al. (2004), non-dimensional conditions range between $300 < We < 900$ and $0.3 < \delta < 1.1$, which are again similar to conditions considered here ($We = 428$, 722, and $\delta = 0.7$).

The measured temporal variation of mean drop size, number, and velocity is expected to be a function of the field of view. In Cossali et al. (2004), the 2D field of view of the shadowgrams is approximately 26 mm wide by 22.5 mm high (Cossali 2013). On the other hand, for the DIH results reported here, the total 3D field of view is effectively 36 mm wide by 24 mm high by 200 mm deep. To approximately match the field of view of Cossali et al. (2004), the results reported in this subsection are taken from the detected drops which fall within a 3D cylindrical region 26 mm diameter in the x–z plane and 22.5 mm high in the y-direction. This cylindrical region is centered at x_0, z_0 with the base coincident with the top of the film. Note, results in Cossali et al. (2004), taken from 2D images, do not resolve the out-of-plane z-direction reported here; nevertheless, due to process symmetry, results for mean drop size and temporal evolution of drop number should agree.

Figure 7 shows the mean number of drops detected from each hologram. Here, symbols show the mean number of detected drops, while the error bars show the minimum and maximum from all realizations and are an indication of process variability. Figure 7 can be compared with Fig. 18 in Cossali et al. (2004). In both cases, the maximum number of drops is detected at around $\tau \approx 2.0$.

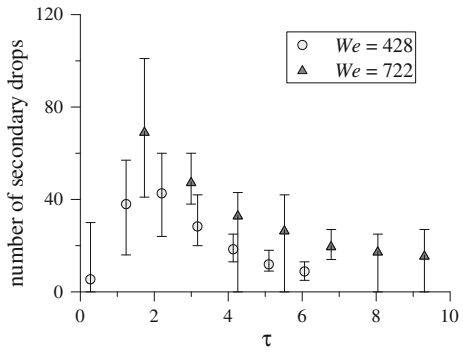

Fig. 7 Number of secondary drops within the 3D volume corresponding to the field of view used in Cossali et al. (2004); *symbols* give the average from all realizations, while *error bars* show the min and max

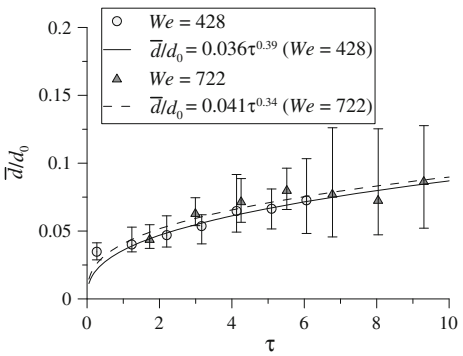

Fig. 8 Dimensionless mean drop diameter, $\bar{d}/d_0$, within the 3D volume corresponding to the field of view used in Cossali et al. (2004); *symbols* give the average from all realizations, while *error bars* show the min and max; *lines* show a power law fit to the experimental data (results for $We = 428$, *solid line*, do not consider the first data point at $\tau = 0.3$)

Figure 8 shows the mean secondary droplet diameter detected from each hologram. Again, symbols show the average value from all realizations, while error bars quantify the minimum and maximum. Figure 8 can be compared with Fig. 16 in Cossali et al. (2004), where it is observed that at $\tau = 1$, $d/d_0 \approx 0.03$ and at $\tau = 10$, $\bar{d}/d_0 \approx 0.1$, for $We > 300$. Comparison of these values with Fig. 8 indicates that the overall change in magnitude of $\bar{d}/d_0$ for the range of τ considered here agrees well with the values reported by Cossali et al. (2004).

As suggested by Cossali et al. (2004), the ensemble average $\bar{d}/d_0$ is fit to a power law relation of the form $\bar{d}/d_0 = q\tau^n$ where q and n are constants. For $We = 428$, the best fit is given by $\bar{d}/d_0 = 0.036\tau^{0.39}$, with a coefficient

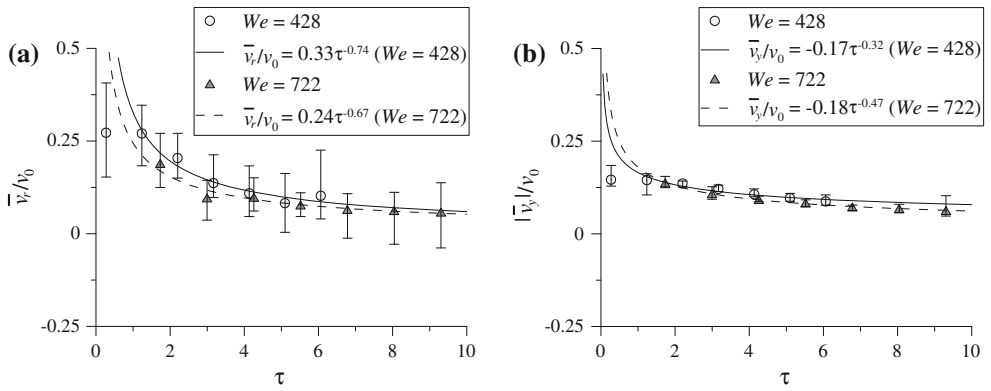

Fig. 9 Dimensionless mean **a** radial velocity, $\bar{v}_r/v_0$, and **b** *y*-velocity, $\bar{v}_y/v_0$, within the 3D volume corresponding to the field of view used in Cossali et al. (2004); *symbols* give the average from all realizations, while *error bars* show the min and max; *lines* show a power law fit to the experimental data (results for $We = 428$, *solid line*, do not consider the first data point at $\tau = 0.3$)

of determination of $R^2 = 0.98$. (Note, this fit disregards the first data point at $\tau = 0.3$. Inclusion of this data point results in a significant decrease in R^2 indicating that drop diameters at early times may show different behavior). Likewise, for $We = 722$, the best fit is given by $\bar{d}/d_0 = 0.041\tau^{0.34}$, with $R^2 = 0.84$. Similarly, Cossali et al. (2004) give a power law fit to their experimental data, and interpolation from values presented in that work predicts that $n \approx 0.33$ and 0.60 at $We = 428$ and 722, respectively. Comparison of the values of n measured here and those given by Cossali et al. (2004) indicates good agreement at $We = 428$. However, agreement is poor at $We = 722$. Possible explanations for this disagreement may be experimental uncertainty, physical scatter in the value of $\bar{d}/d_0$ combined with insufficient data for converged statistics, or inappropriateness of the power law relation.

Finally, measured *x*–*z* droplet positions and velocities are converted to radial positions, *r*, and velocities, v_r, by taking the measured mean droplet positions (x_0, z_0) as the origin. From this, Fig. 9 shows the evolution of the mean radial- and *y*-velocities. Power law fits of the form $\bar{v}/v_0 = q\tau^n$ are provided. For $We = 428$, the best fits are given by $\bar{v}_r/v_0 = 0.33\tau^{-0.74}$, with $R^2 = 0.93$, and $\bar{v}_y/v_0 = -0.17\tau^{-0.32}$, with $R^2 = 0.92$, once again disregarding the first data point at $\tau = 0.3$, which does not appear to follow the same trends. Likewise, for $We = 722$, the best fits are given by $\bar{v}_r/v_0 = 0.24\tau^{-0.67}$, with $R^2 = 0.94$, and $\bar{v}_y/v_0 = -0.18\tau^{-0.47}$, with $R^2 = 0.997$. Due to challenges measuring these quantities with alternative techniques, little experimental data are available in the literature for direct comparison. However, in their model, Yarin and Weiss (1995) predict the crown radius scales with $n = 1/2$ power with respect to time. This was confirmed by Cossali et al. (2004) who experimentally measured temporal scaling of the crown radius and found $n \approx 0.4$ to 0.5 (equivalently, crown radial velocity scales like $n \approx -0.6$ to -0.5). Here, the scaling of secondary droplet radial velocities shows similar trends which support an assumption that the radial velocities of secondary droplets are largely determined by the radial velocity of the crown. Similar relations between the temporal evolution of crown height and initial *y*-velocities are also likely; however, due to the relative complexity of models for crown height (Roisman and Tropea 2002), comparison with the measured *y*-velocities is left for future work.

5 Conclusions

An experimental investigation of droplet impact on a thin film is presented. For the first time, digital in-line holography (DIH) and the hybrid method of particle detection are applied to measure the three-dimensional (3D) size, position, and velocity of secondary droplets. In addition, the power of DIH to measure the complex 3D morphologies of the protruding jets is demonstrated. Specific conclusions include

- DIH is well suited for quantitative diagnostics of 3D multiphase particulate flows, especially those involving sparse particle fields and dynamic events for which continuous point measurements are challenging.
- For the current application, the hybrid particle detection method is shown to yield secondary drop size distributions which approach zero at the limit of large and small diameters, indicating that all relevant drop sizes have been captured.
- Reconstructed velocity vectors display the expected symmetry and good agreement between the in-plane and out-of-plane components.
- Flow symmetry provides an effective means to quantify depth uncertainty from experimental holograms. Here, depth uncertainty is found to be approximately 0.7 of the mean droplet diameter.

- Experimental results for the temporal evolution of drop number, size, and velocity are in good agreement with previous experiments and theories.
- The temporal scaling of secondary droplet radial velocities follows trends similar to those predicted for the radial velocity of the crown, indicating droplet radial velocities may be largely determined by the crown radial velocity.

Acknowledgments The authors would like to thank Bion Shelden for assistance with the initial setup and Alexander L. Brown for a thorough review of the manuscript. Both are from Sandia National Laboratories, which is a multiprogram laboratory operated by Sandia Corporation, a Lockheed Martin Company, for the United States Department of Energy's National Nuclear Security Administration under contract No. DE-AC04-94AL85000.

References

Cossali GE (2013) Personal communication

Cossali GE, Marengo M, Coghe A, Zhdanov S (2004) The role of time in single drop splash on thin film. Exp Fluids 36(6):888–900. doi:10.1007/s00348-003-0772-0

Gao J, Guildenbecher DR, Reu PL, Chen J (2013a) Uncertainty characterization of particle depth measurement using digital in-line holography and the hybrid method. Opt Express 21(22)

Gao J, Guildenbecher DR, Reu PL, Kulkarni V, Sojka PE, Chen J (2013b) Quantitative, 3D diagnostics of multiphase drop fragmentation via digital in-line holography. Opt Lett 38(11):1893–1895

Gire J, Denis L, Fournier C, Thiébaut E, Soulez F, Ducottet C (2008) Digital holography of particles: benefits of the 'inverse problem' approach. Meas Sci Technol 19(7):074005

Gopalan B, Katz J (2010) Turbulent shearing of crude oil mixed with dispersants generates long microthreads and microdroplets. Phys Rev Lett 104(5):054501

Guildenbecher DR, Gao J, Reu PL, Chen J (2012) Digital holography reconstruction algorithms to estimate the morphology and depth of non-spherical, absorbing particles. In: SPIE Optical Engineering + Applications, San Diego, CA, 2012. SPIE

Guildenbecher DR, Gao J, Reu PL, Chen J (2013a) Digital holography simulations and experiments to quantify the accuracy of 3D particle location and 2D sizing using a proposed hybrid method. Appl Opt 52(16):3790–3801

Guildenbecher DR, Reu PL, Gao J, Chen J (2013b) Experimental methods to quantify the accuracy of 3D particle field measurements via digital holography. In: Digital Holography and 3-D Imaging, Kohala Coast, Hawaii, 2013b. OSA

Katz J, Sheng J (2010) Applications of holography in fluid mechanics and particle dynamics. Annu Rev Fluid Mech 42:531–555. doi:10.1146/annurev-fluid-121108-145508

Khanam T, Nurur Rahman M, Rajendran A, Kariwala V, Asundi AK (2011) Accurate size measurement of needle-shaped particles using digital holography. Chem Eng Sci 66(12):2699–2706. doi:10.1016/j.ces.2011.03.026

Lebrun D, Allano D, Méès L, Walle F, Corbin F, Boucheron R, Fréchou D (2011) Size measurement of bubbles in a cavitation tunnel by digital in-line holography. Appl Opt 50(34):H1–H9

Meng H, Pan G, Pu Y, Woodward SH (2004) Holographic particle image velocimetry: from film to digital recording. Meas Sci Technol 15(4):673

Moreira ALN, Moita AS, Panão MR (2010) Advances and challenges in explaining fuel spray impingement: how much of single droplet impact research is useful? Prog Energy Combust Sci 36(5):554–580. doi:10.1016/j.pecs.2010.01.002

Okawa T, Shiraishi T, Mori T (2006) Production of secondary drops during the single water drop impact onto a plane water surface. Exp Fluids 41(6):965–974. doi:10.1007/s00348-006-0214-x

Richter B, Dullenkopf K, Bauer HJ (2005) Investigation of secondary droplet characteristics produced by an isooctane drop chain impact onto a heated piston surface. Exp Fluids 39(2):351–363. doi:10.1007/s00348-005-1018-0

Roisman IV, Tropea C (2002) Impact of a drop onto a wetted wall: description of crown formation and propagation. J Fluid Mech 472:373–397. doi:10.1017/S0022112002002434

Samenfink W, Elsäßer A, Dullenkopf K, Wittig S (1999) Droplet interaction with shear-driven liquid films: analysis of deposition and secondary droplet characteristics. Int J Heat Fluid Flow 20:462–469

Schnars U, Jueptner W (2005) Digital holography: digital hologram recording, numerical reconstruction, and related techniques. Springer, Berlin

Spuler SM, Fugal J (2011) Design of an in-line, digital holographic imaging system for airborne measurement of clouds. Appl Opt 50(10):1405–1412

Tian L, Loomis N, Domínguez-Caballero JA, Barbastathis G (2010) Quantitative measurement of size and three-dimensional position of fast-moving bubbles in air-water mixture flows using digital holography. Appl Opt 49(9):1549–1554

Tinevez J-Y (2012) Simple tracker. http://www.mathworks.com/matlabcentral/fileexchange/34040-simple-tracker. Accessed December 1 2012

Wu Y, Wu X, Wang Z, Chen L, Cen K (2011) Coal powder measurement by digital holography with expanded measurement area. Appl Opt 50(34):H22–H29

Yang Y, Li G, Tang L, Huang L (2012) Integrated gray-level gradient method applied for the extraction of three-dimensional velocity fields of sprays in in-line digital holography. Appl Opt 51(2):255–267

Yarin AL (2006) Drop impact dynamics: splashing, spreading, receding, bouncing…. Annu Rev Fluid Mech 38(1):159–192. doi:10.1146/annurev.fluid.38.050304.092144

Yarin AL, Weiss DA (1995) Impact of drops on solid surfaces: self-similar capillary waves, and splashing as a new type of kinematic discontinuity. J Fluid Mech 283:141–173. doi:10.1017/S0022112095002266